Toward Autonomous Mapping with AUVs - Line-to-Line Terrain Navigation

Ove Kent Hagen, Kjetil Bergh Ånonsen and Torstein Olsmo Sæbø
Norwegian Defence Research Establishment (FFI)
P O Box 25, NO-2027 Kjeller, Norway
Email: ove-kent.hagen@ffi.no

***Abstract*—In autonomous mapping surveys the autonomous underwater vehicle (AUV) cannot rely on receiving position aiding from a surface vehicle or any other external infrastructure. The AUV can however use any payload sensor to restrict the position error drift in the navigation system. In this paper we consider using the bathymetric sensor in line-to-line terrain navigation. Terrain navigation will limit position error growth, and also ensure enough overlap between the lines such that the survey area is covered. We show that sparse map coverage from a line of bathymetry leads to a bias when used in a straightforward implementation of the point mass filter terrain navigation algorithm, and we develop a modification to the algorithm that handles this robustly. The algorithm achieves good performance when tested off-line on real data from a HUGIN AUV equipped with the HISAS 1030 interferometric synthetic aperture sonar.**

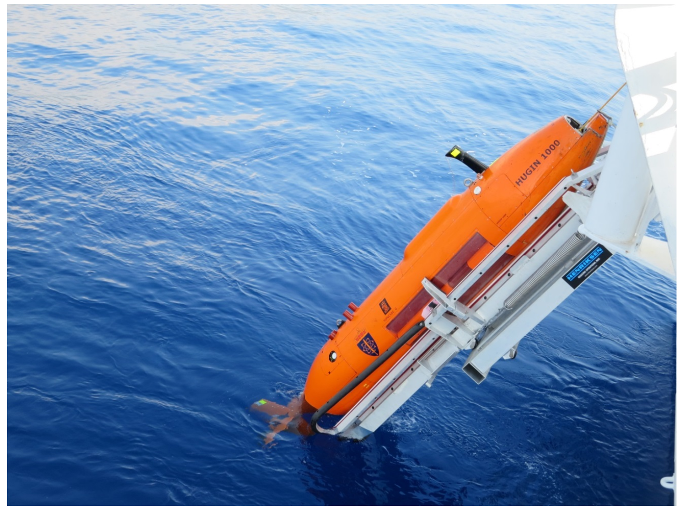

Fig. 1. The HISAS 1030 mounted on a HUGIN 1000-MR AUV during launch.

I. Introduction

Accurate bathymetric mapping has been an essential capability of Autonomous Underwater Vehicles (AUVs) ever since the introduction of these vehicles into commercial deep water surveys. To accurately georeference bathymetric measurements of the sea floor, accurate navigation is a basic requirement. Today these surveys are usually done with a surface ship equipped with a high-accuracy GPS system, continuously tracking the AUV with an acoustic ultra-short-baseline (USBL) system throughout the mission. By integrating the GPS-USBL underwater position measurements with the low drift inertial navigation system (INS) typically found on these AUVs, the position accuracy requirement is usually met, after post-processing the navigation data [1].

An AUV that maps an area autonomously cannot depend on the surface ship except possibly in the periods of launch and recovery. The navigation of the AUV then becomes a major challenge. If the water is shallow enough, frequent GPS-fixes at the surface may suffice, and if there is infrastructure like navigation transponders nearby, those can also be used. However, no general solution exists for these scenarios today. A completely autonomous solution is to use any payload sensor carried by the AUV to improve its navigation, such as multibeam echo sounders, imaging sonars, or cameras. In this article we only consider the bathymetric sensors of the AUV. Terrain navigation is now an established technique for subsurface position updates of AUVs. By comparing bathymetric measurements with an a priori known digital terrain model (DTM) of the sea floor, the best matching position may be used to update the navigation system of the AUV. This has been shown by several authors to efficiently bind the position error of AUVs in suitable terrain [2]–[5].

The major drawback of this navigation technique is the requirement that a DTM must be available before the start of the AUV mission. This is especially obvious if the mission of the AUV is to do a bathymetric survey of an unknown area. A solution to this problem is to apply the popular technique from robot navigation called Simultaneous Localization And Mapping (SLAM), which also has been adopted for the case of bathymetric mapping [6]. In this technique both the terrain referenced position of the AUV and the map created by the AUV are updated simultaneously in a common estimator. If the AUV is equipped with a low drift navigation system, another technique similar to SLAM is possible, in which the problem is separated, local mapping first and then localization within the local map, within the same mission [7], [8]. This will instead give a relative position measurement that can be passed back to the navigation system, and also used to update parameters for the local maps [7].

In this article we explore the use of terrain navigation

978-0-933957-43-5 ©2015 MTS

TABLE I

TYPICAL HISAS 1030 SYSTEM SPECIFICATIONS.

Center frequency [kHz]	100
Wavelength [cm]	1.5
Bandwidth [kHz]	30
Frequency range [kHz]	85-115
Along-track image resolution [cm]	3
Cross-track image resolution [cm]	3
Maximum range at 2 m/s [m]	175
Area coverage rate [km^2/h]	2
Interferomtric baseline [cm]	28
Interferomtric baseline [wavelengths]	18.7

to lower position drift in a specific bathymetric survey-pattern without an a priori known DTM. Real data from a HUGIN AUV equipped with a HISAS 1030 interferometric synthetic aperture sonar (SAS) are used in the post-processing tests. From each survey-line we use interferometric SAS- and sidescan sonar (SSS) processing to create reference bathymetry. In the consecutive survey-lines the overlaps are processed by a Bayesian line-to-line terrain navigation algorithm, estimating relative position measurements and corresponding accuracies for the INS. The grid-based terrain navigation algorithm used by the HUGIN AUV is modified herein to deal with the problem when we are missing map information. This is a problem that occurs when parts of the grid do not get any, or not enough, information back from the DTM. This may be because the AUV is near the edge of the DTM, or there are holes in the DTM [9].

In Section II the HISAS 1030 system, and the interferometric processing is described in more detail. Modifications to a Bayesian terrain navigation algorithm dealing with the problem of sparse DTM coverage are developed in Section III. Some preliminary results on data from a HUGIN AUV are shown in Section IV, before conclusion and future work are summarized in Section V.

II. HISAS 1030

The primary sensor on the HUGIN AUV is the HISAS 1030 synthetic aperture sonar [10]. The HISAS 1030 is a two-sided broadband long-baseline interferometric sonar, which was primarily developed for very high resolution seafloor imaging, but with its two vertically separated receivers (on each side) it is also capable of bathymetric measurements. The HISAS 1030 delivers two-sided synthetic aperture sonar imagery with around 3x3 cm resolution and 175 meters range at nominal HUGIN speed. Figure 1 shows a picture of the HISAS 1030 mounted on a HUGIN AUV during launch while Table I summarizes typical system specifications.

A. Bathymetric measurements using HISAS 1030

The HISAS 1030 can produce bathymetric measurements using interferometric processing (also called swath bathymetry [11]). Figure 2 shows a sketch of the principle. Sidescan or SAS images are beamformed on two vertically separated receive arrays (Rx1 and Rx2 in the figure). The images are

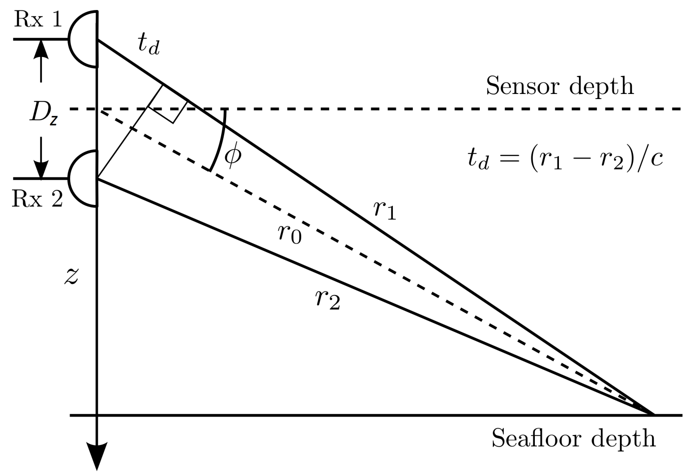

Fig. 2. Sketch of the interferometric principle using two vertically separated receive arrays.

coregistered [12] and from the phase differences between the images we estimate a difference in time-of-flight, t_d, which again relates to the path difference of the recorded sound wave. Simple trigonometry then yields

$$z = r\frac{ct_d}{D_z}, \tag{1}$$

where z is the bathymetric estimate, r the range, c the sound speed and D_z the baseline between the receive arrays.

B. Coarse sidescan (swath) bathymetry

The HISAS 1030 can produce two different bathymetric products: Bathymetry based on sidescan lines and bathymetry based on SAS images. Sidescan bathymetry is a ping-by-ping product. For each transmitted pulse, a single *slant-range* beam is formed. Then the beams are co-registered by re-sampling them onto a common *ground-plane* [13]. From the co-registered beams, patches of length L are correlated for a large number of ranges. The maximum correlation coefficient gives us an estimate of the coherence μ and time-delay δt.

The estimated coherence, μ can be converted to an equivalent SNR, ρ

$$\rho = \frac{\mu}{1-\mu}. \tag{2}$$

The Cramer-Rao lower bound (CRLB) of the time-delay estimate can be found from the signal-to-noise ratio (SNR) and the number of independent samples, N, used in the correlation window [13]–[15]. Figure 3 shows the relative depth accuracy for a few relevant SNRs and a correlation window of $L = 3.2$ meters ($N = 93$), which is also what we have used to generate the results presented in this article.

The horizontal resolution, dx, in sidescan bathymetry is given by sidescan resolution along-track

$$dx = 0.88\frac{\lambda}{D_x}r, \tag{3}$$

where λ is the signal wavelength and D_x the along-track array length. The HISAS has a signal wavelength of 15 mm (100

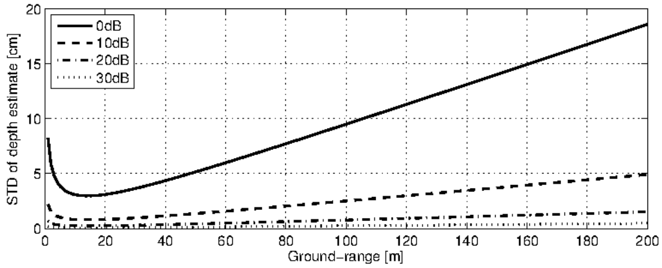

Fig. 3. The figure shows the standard deviation of the depth estimate as a function of range using sidescan bathymetry on HISAS 1030. The different curves indicate different SNRs.

kHz) and an array length of 1.2 meters. This corresponds to 0.55 meters resolution at 50 meters range, 1.1 meters at 100 meters and 2.2 meters at maximum range (200 meters). The across-track resolution is given by the 3.2 meters correlation window.

C. High resolution SAS bathymetry

SAS *interferometry* is in principle very similar to sidescan bathymetry. The main difference is the input data: SAS images instead of single-ping sidescan lines. This means that instead of estimating the bathymetry on individual beams which may point in slightly different directions, the bathymetry is estimated on rectangular earth-fixed grids of a few by a few hundred meters. The coregistration onto ground-range is identical for sidescan and SAS bathymetry, so are the equations that relate time-delay and relative depth. However, the correlation step is slightly different: We use a two-dimensional correlation window, which is only correlated along the range direction [16]

Instead of using the CRLB to assess the depth accuracy, we integrate the marginal probability density function of the interferometric phase difference [12], [17]. According to [12] the CRLB is a better model for a speckle scene – the case for a SAS image of a general seafloor. However, for large correlation windows and positive SNRs, the difference between the CRLB and integrating the marginal probability density function is neglectable. Figure 3 therefore also illustrates the accuracy of SAS interferometry given the same number of independent samples in each estimate.

The horizontal resolution is the primary difference between sidescan bathymetry and SAS bathymetry. The bathymetric resolutions are now given by the correlation window size in both dimension. The data presented in this article were generated using correlation windows of 18 by 18 cm which corresponds to $N = 27.5$. Since the theoretical accuracy is proportional to $1/\sqrt{N}$, the accuracy in this case becomes a factor of 1.8 worse than the accuracies presented in Figure 3, but the resolutions are 18 times better across-track and 3-12 times better along-track.

III. Bayesian line-to-line terrain navigation

The high accuracy requirement of navigation in a mapping scenario is mainly after post-processing. This means that more computational complex algorithms may be used off-line after the mission, and in particular the use of the SAS bathymetry may be considered. In real-time the navigation accuracy requirement is just to ensure that the overlap between consecutive lines are large enough to enable line-to-line terrain navigation, which then automatically ensures that the survey area is covered. By using the bathymetric mapping sensors in terrain navigation, and fusing these with the navigation system, a self-consistent map of the target area can be made [7].

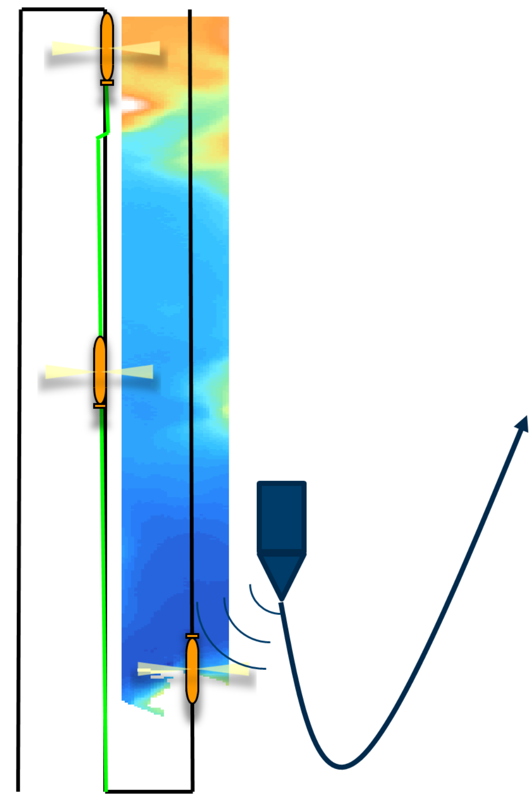

Fig. 4. The surface vessel tracks the AUV on the first line, and thereafter the AUV maps the survey area autonomously, using line-to-line terrain navigation to ensure complete coverage.

Line-to-line terrain navigation alone can only improve the navigation in a relative sense. The absolute (global) position of the mapped area will therefore be constrained by mapping some globally referenced lines of bathymetry as well. The pattern for these lines will depend on the scenario, one example is shown in Figure 4. In that case the surface vehicle follows the AUV on the very first line, acoustically tracking it with its GPS-USBL system. Thereafter the AUV navigates autonomously using line-to-line terrain navigation to limit the position error growth. On the last line the surface vehicle may even return tracking the AUV before recovery, and through navigation post-processing the global positioning of the last line will also improve the overall navigation in the survey area.

Terrain navigation is loosely integrated with the INS in the HUGIN AUV [5]. In this system the terrain navigation algorithm receives updates of the estimated motion from the INS, and correlates bathymetric measurements with the DTM until a convergence/divergence criterion is met. In case of convergence an integrity system checks if the solution is valid, and can be fed back to the INS. The system proposed herein differs in that line-to-line terrain navigation will only give position updates relative to the previous line. In general these must be integrated as a relative position update to the INS, called macro-delta position measurements in the HUGIN INS [18]. The integration of these measurements with the INS is beyond the scope of this article. The reference lines with global positioning can however be used in a regular manner by the INS.

A. Mathematical Model

Only the measurement model of the problem is presented here, for a more complete description, see e.g. [19]. Let $\boldsymbol{x}_k = (x_k, y_k, z_k)$ denote the AUV's position at time $t = t_k$ in a local north-east-down system. At time t_k the AUV measures a bathymetric profile consisting of m_k measurements, denoted by the set of vectors $(\boldsymbol{\xi}_k, \boldsymbol{\eta}_k, \boldsymbol{\zeta}_k) = \{(\xi_{k,i}, \eta_{k,i}, \zeta_{k,i})\}_{i=1}^{m_k}$. We assume the bathymetry is given by the scalar function $h(\boldsymbol{x}) = h(x, y)$, which outputs sea floor depth at position $\boldsymbol{x}$. The measurement model is then given by

$$\boldsymbol{\zeta}_k = \boldsymbol{h}_k(\boldsymbol{x}_k) + \boldsymbol{w}_k. \tag{4}$$

The measurement vector function in (4) $\boldsymbol{h}_k(\boldsymbol{x}_k) = \{h_{k,i}\}_{i=1}^{m_k}$ has scalar components

$$h_{k,i} = h(x_k + \xi_{k,i}, y_k + \eta_{k,i}) - z_k. \tag{5}$$

The measurement noise $\boldsymbol{w}_k$ is assumed to be zero-mean, white and Gaussian distributed, and models both the sensor and DTM errors. The level of this noise is calculated based on the sensor accuracy indicated in Figure 3.

B. Measurement update

HUGIN's terrain navigation system uses a nonlinear Bayesian estimator, called a point mass filter (PMF) [20]. The filter calculates the probability density function (PDF) of the position error on a floating grid G_k around the current INS solution. The PDF diffuses on the grid according to the estimated drift in the INS solution between the pings [19], and for each ping the PDF is updated according to Bayes' theorem

$$p(\boldsymbol{x}_k|\boldsymbol{Z}_k) = \beta_k^{-1} p(\boldsymbol{\zeta}_k|\boldsymbol{x}_k) p(\boldsymbol{x}_k|\boldsymbol{Z}_{k-1}), \tag{6}$$

where $\boldsymbol{Z}_k$ denotes the set of all measurements up to time t_k, and β_k is a normalization constant

$$\beta_k = \int_{G_k} p(\boldsymbol{\zeta}_k|\boldsymbol{x}_k) p(\boldsymbol{x}_k|\boldsymbol{Z}_{k-1}) dx_k. \tag{7}$$

Since the measurement noise $\boldsymbol{w}_k$ is zero-mean, white and Gaussian, it is completely described by a covariance matrix $\boldsymbol{C}_k$, and the measurement likelihood function in (6) is then given by

$$p(\boldsymbol{\zeta}_k|\boldsymbol{x}_k) = \frac{1}{\sqrt{(2\pi)^{m_k}|\boldsymbol{C}_k|}} e^{-\frac{1}{2}(\boldsymbol{\zeta}_k - \boldsymbol{h}_k(\boldsymbol{x}_k))^T \boldsymbol{C}_k^{-1}(\boldsymbol{z}_k - \boldsymbol{h}_k(\boldsymbol{x}_k))}. \tag{8}$$

Line-to-line terrain navigation introduces some problems to the regular algorithm. Using only an interferometric sidescan, the survey pattern is designed to fill in the gap directly beneath the AUV, such that every second line in the pattern have large and small overlaps, see Figure 5. Small overlaps inherently increases the probability of observing terrain without much information. In flat terrain there is a well-known problem of false fixes, where the algorithm occasionally calculates high correlations between sensor noise and map noise. In [5] this was solved by possibly rejecting these solutions in an integrity system based on the terrain flatness, but in [21], [22] a more constructive approach was developed in which the likelihood function is exponentially weighted to increase the estimator robustness. The $0 < \alpha(\boldsymbol{x}_k) < 1$ introduced in [22] (a measure of actual terrain information) depends on the terrain variation, map noise and sensor noise, and is calculated for each grid point during measurement update. This method of increasing the likelihood function robustness is implemented by modifying the measurement likelihood function by

$$p_{mod}(\boldsymbol{\zeta}_k|\boldsymbol{x}_k) = p(\boldsymbol{\zeta}_k|\boldsymbol{x}_k)^{\alpha(\boldsymbol{x}_k)}, \tag{9}$$

and is adopted to the variants of the PMF algorithms described herein.
Another problem with the overlaps is that the algorithm will be without map support for large portions of the grid G_k. In [5] the terrain navigation algorithm is reset if any part of the grid is without map support. This is not an option in the scenario of line-to-line terrain navigation.

C. Point Mass Filter with sparse support

We will first give a more precise meaning of map support, and we will omit the time subscript k when it is not necessary. If $\boldsymbol{x}_g \in G$ is a point on the grid, then we will say that $\boldsymbol{x}_g$ has map support if all the measurements $\{\boldsymbol{x}_g + [\xi_i, \eta_i]^T\}_{i=1}^m$ are in the domain of the terrain function $h(\boldsymbol{x})$. Since we are using DTMs based solely on one single survey line at the time, the domain of the terrain function $h(\boldsymbol{x})$ is limited, and typically only offers sparse support in the grid. The derivation of the PMF in [20] assumes the measurement function is everywhere defined, so all modifications to the PMF to deal with the problem of sparse support must be considered ad-hoc within that framework.

Two problems with the sparse support of the point mass filter are recognized. Some grid points will not receive any information at all from the measurements, and an uneven amount of measurements is used to calculate the likelihood function for the different grid points. The first problem can be circumvented by skipping update of the grid points lacking support, while computing the supported grid points in a nearly regular manner. During the renormalization step however, care is taken in normalizing each region while respecting the initial distribution. Let $G_s \subseteq G$ denote the part of the grid with measurement support, and $P(G_s) = \int_{G_s} p(\boldsymbol{x}_k|\boldsymbol{Z}_{k-1})dx_k$ the a priori probability of the AUV being in the supported part of the grid, then the normalization in (7) is modified to

$$\beta_k = \frac{1}{P(G_s)} \int_{G_s} p(\boldsymbol{\zeta}_k|\boldsymbol{x}_k)p(\boldsymbol{x}_k|\boldsymbol{Z}_{k-1})dx_k. \tag{10}$$

D. Regular log-likelihood

The second problem is that the number of measurements is not the same for each supported grid point. Let m denote the number of measurements, and let $m(\boldsymbol{x}) <= m$ denote the number of measurements supported by the grid point $\boldsymbol{x}$. Let $U(\boldsymbol{x})$ be an $m(\boldsymbol{x})\times m$ subsampling matrix at grid point $\boldsymbol{x}$, that picks out only those measurements that have support, i.e such that $\delta(\boldsymbol{x}) = U(\boldsymbol{x})(\boldsymbol{\zeta} - h(\boldsymbol{x}))$ have full support. The covariance matrix of $\delta(\boldsymbol{x})$ is then given by $\boldsymbol{C}(\boldsymbol{x}) = U(\boldsymbol{x})\boldsymbol{C}U(\boldsymbol{x})^T$. A straightforward modification of the PMF is then to compute the log-likelihood of (8) as

$$\begin{aligned} \log p(\boldsymbol{\zeta}|\boldsymbol{x}) \quad &= \quad -\frac{1}{2}\boldsymbol{\delta}(\boldsymbol{x})^T\boldsymbol{C}(\boldsymbol{x})^{-1}\boldsymbol{\delta}(\boldsymbol{x}) \\ &\quad -\frac{1}{2}\log|\boldsymbol{C}(\boldsymbol{x})| - \frac{1}{2}\log 2\pi^{m(\boldsymbol{x})} \end{aligned} \tag{11}$$

This straightforward modification will be referred to as PMF-reg.

E. Measurement normalization of the log-likelihood

The modification in (11) may seem reasonable, but can be shown to fail consistently in special cases. Since $\boldsymbol{C}(\boldsymbol{x})$ is a real positive definite symmetric matrix $\det(\boldsymbol{C}(\boldsymbol{x})) = \prod_{i=1}^{m(\boldsymbol{x})} \lambda_i$, where $\lambda_i > 0$ are the eigenvalues of $\boldsymbol{C}(\boldsymbol{x})$. We can also compute the Cholesky decomposition $\boldsymbol{C}(\boldsymbol{x}) = \boldsymbol{S}(\boldsymbol{x})\boldsymbol{S}(\boldsymbol{x})^T$, and introduce $\epsilon(\boldsymbol{x}) = \boldsymbol{S}(\boldsymbol{x})^{-1}\boldsymbol{\delta}(\boldsymbol{x})$. If $\boldsymbol{x}$ is the true position of the AUV, then $\boldsymbol{\epsilon}(\boldsymbol{x})$ is standard normally distributed, which implies that

$$\boldsymbol{\epsilon}(\boldsymbol{x})^T\boldsymbol{\epsilon}(\boldsymbol{x}) = \boldsymbol{\delta}(\boldsymbol{x})^T\boldsymbol{C}(\boldsymbol{x})^{-1}\boldsymbol{\delta}(\boldsymbol{x}) \sim \chi^2_{m(\boldsymbol{x})} \tag{12}$$

is chi-square distributed with $m(\boldsymbol{x})$ degrees of freedom. Let $E[\cdot]$ denote the expectation operator with respect to the measurement error PDF, then

$$E[\log p(\boldsymbol{\zeta}|\boldsymbol{x})] = -\frac{1}{2}m(\boldsymbol{x}) - \frac{1}{2}\sum_{i=1}^{m(\boldsymbol{x})}\log\lambda_i - \frac{m(\boldsymbol{x})}{2}\log 2\pi, \tag{13}$$

which shows the dependency on the number of measurements in the expected log-likelihood function at the true position. The same argument can however be made near any local maximum on the grid. This causes a problem that is most easily seen in the special case of a flat sea floor $h(\boldsymbol{x}) \equiv h_0$ and uncorrelated measurements with constant variance, i.e. $\lambda_i = \lambda$, then for any point on the grid (13) becomes

$$E[\log p(\boldsymbol{\zeta}|\boldsymbol{x})] = -\frac{1}{2}m(\boldsymbol{x})(1 + \log\lambda + \log 2\pi). \tag{14}$$

In this case the expected log-likelihood varies linearly with the number of supported measurements on the grid, even though the sea floor is flat and without any actual information useful for terrain navigation. The form of the bias in (14) motivates multiplying the log-likelihood with $1/m(\boldsymbol{x})$. This is equivalent to modifying the likelihood function by

$$p_{mod}(\boldsymbol{\zeta}_k|\boldsymbol{x}_k) = p(\boldsymbol{\zeta}_k|\boldsymbol{x}_k)^{\frac{\alpha(\boldsymbol{x})}{m(\boldsymbol{x})}}. \tag{15}$$

This effectively removes the bias in the flat sea floor scenario, but as a side-effect it also increases the measurement and map variance in general. This modification with measurement normalization will be referred to as PMF-nrm. Interestingly this (ad-hoc) bias removing implementation of the measurement likelihood function within the Bayesian framework, is tightly connected to the normalized correlation measure used to register sub-maps in [7].

IV. Preliminary results

The Norwegian Defence Research Establishment (FFI) conducted a series of missions with the HUGIN HUS AUV to explore survey patterns for autonomous mapping. The HUGIN HUS has a low-drift INS, based on a navigation grade IMU (Honeywell HG9900), and is aided by a Doppler velocity log (Teledyne RDI WHN 300) and a high quality pressure sensor (Paroscientific DigiQuatz). Since the IMU is accurate enough for gyrocompassing, the AUV's attitude is known accurately enough, and depth is accurately computed based on the pressure sensor when compensated for atmospheric pressure, tide and density variations in the water column. If not aided by any position measurements the INS will start to drift in horizontal position. HUGIN HUS has a real-time terrain navigation system, but the system does not yet support the line-to-line scenario described in this article. During the missions the AUV was tracked on the GPS-USBL on board FFI's research vessel H.U. Sverdrup II, and occasionally the AUV received GPS-USBL position updates in real-time to simulate updates from a terrain navigation system. This guaranteed sufficient overlap between the lines. The GPS-USBL measurements were also used in the navigation post-processing with NavLab [23] to create a reference solution.

A. Line-to-line terrain navigation

The terrain navigation algorithms are compared for an example of both types of lines, with small (line l03) and large (line l04) overlaps as shown in Figure 5. Only the interferometric sidescan sonar processing is used as measurement input to the PMF. The PMF grid is 15 meters x 15 meters wide with 25 cm resolution, and use the post-processed navigation solution as origin. The initial PDF was modeled as Gaussian distributed with 3 meters standard deviation in both north and east. The correlation sequence is reset after 25 pings. Convergence is checked using criteria based on the estimated PDF having large enough Kullback-Leibler divergence from the initial PDF, and having similarities to a Gaussian PDF [24] such that the position could be used by the INS. The post-processed navigation solution was used as input to the PMF in these tests,

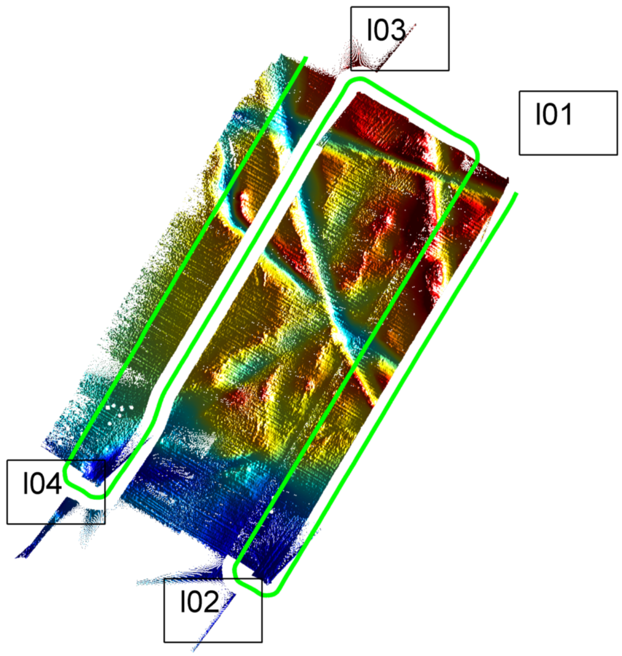

Fig. 5. Overview of the start of the survey pattern for the side-looking bathymeter. The SSS bathymetry of line l04 is not shown, to indicate how these measurements will infill the gap from line l03.

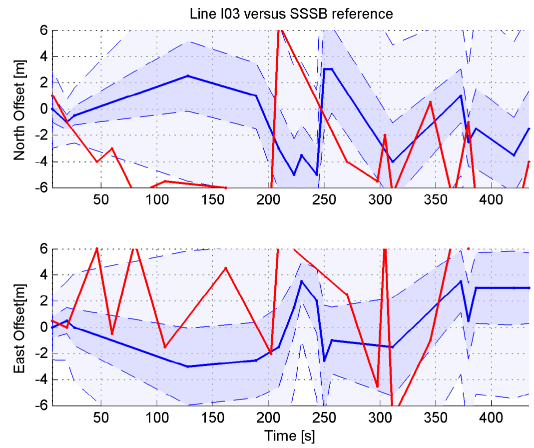

Fig. 6. Line l03: terrain navigation offset and confidence levels using PMF-nrm with SSSB reference data from line l02 (blue), and the corresponding results from PMF-reg (red).

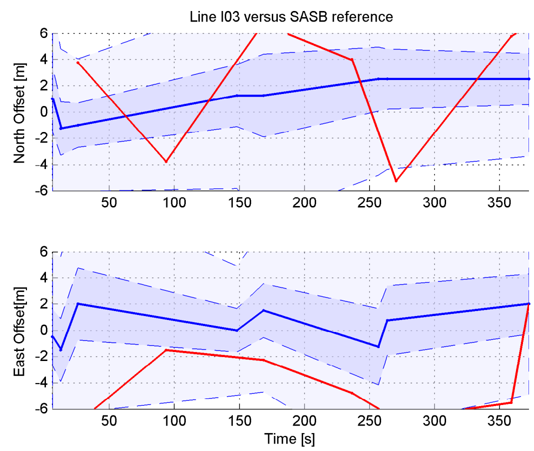

Fig. 7. Line l03: terrain navigation offset and confidence levels using PMF-nrm with SASB reference data from line l02 (blue), and the corresponding results from PMF-reg (red).

since we are only interested in the achievable performance of terrain navigation. The reference line bathymetry and accuracy maps are created based on both sidescan sonar (SSSB) and synthetic aperture sonar (SASB) in this comparison. Figure 6 shows the comparison between PMF-reg and PMF-nrm in line l03 with a small overlap to the SSSB reference line l02, and Figure 7 shows the corresponding comparison using the SASB reference from line l02. The PMF-nrm gives a much more consistent and stable result than PMF-reg. The performance of PMF-nrm is comparable between using SSSB and SASB as reference, but more terrain navigation fixes are obtained using SSSB. This is probably due to the fact that the practical range of the SSSB is larger then SASB, which leads to larger overlaps between the lines. Similarly, Figure 8 shows the comparison between the algorithms in line l04 with a large overlap to the SSSB reference line l03, and Figure 9 shows the corresponding comparison using the SASB reference from line l03. Again the PMF-nrm shows consistently high performance, with more terrain navigation fixes using the SSSB reference. PMF-reg is again largely unstable, except for the periods where the confidence levels of PMF-nrm are tight. This is in regions where the terrain has more variation. This is exactly as would be expected from the analysis in Section III-E, the problem is expected to be most significant in regions with nearly flat terrain.

B. *Self-consistent bathymetry*

The similar PMF results from line l02 with SSSB reference from line l01 is given in Figure 10. This line has large overlap, which is also reflected in the tight confidence interval, but there is a notable increasing bias in the north direction. The tests showed a similar trend using the SASB reference, and we suspect it may be caused by a biased error in the GPS-USBL position used by the automated navigation post-processing. We reprocessed the navigation with NavLab using the terrain navigation measurements instead, and compared the maps based on both lines and the two position sources in the navigation post-processing. A part of the result is shown in Figure 11, where there are signs of inconsistency in the fused bathymetry form line l02 and l03 when using GPS-USBL, that are not present when using line-to-line terrain navigation. This shows that terrain navigation can increase the self-consistency of the survey map, even in the standard survey scenario when the AUV is tracked on GPS-USBL by the surface vessel.

V. Conclusion and future work

We have developed modifications to the PMF algorithm for use in a line-to-line terrain navigation scenario. The preliminary results indicate a great improvement using a

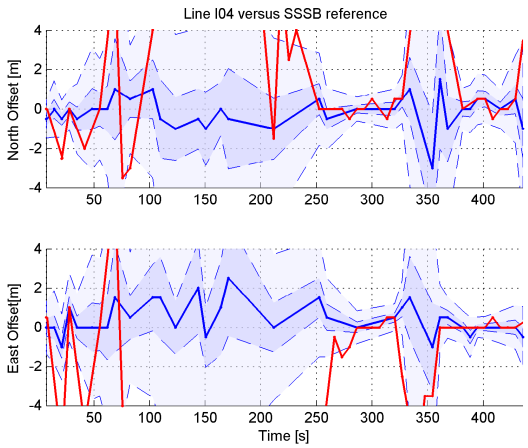

Fig. 8. Line l04: terrain navigation offset and confidence levels using PMF-nrm with SSSB reference data from line l03 (blue), and the corresponding results from PMF-reg (red).

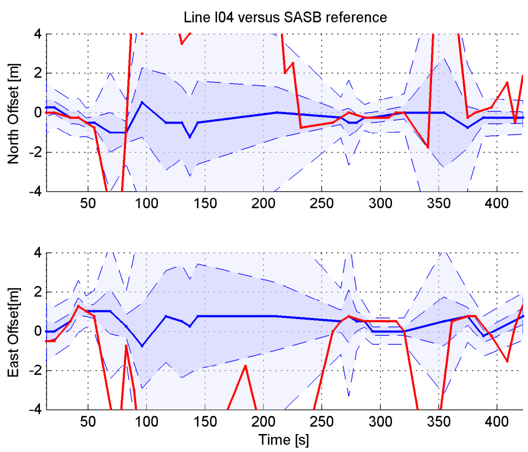

Fig. 9. Line l04: terrain navigation offset and confidence levels using PMF-nrm with SASB reference data from line l03 (blue), and the corresponding results from PMF-reg (red).

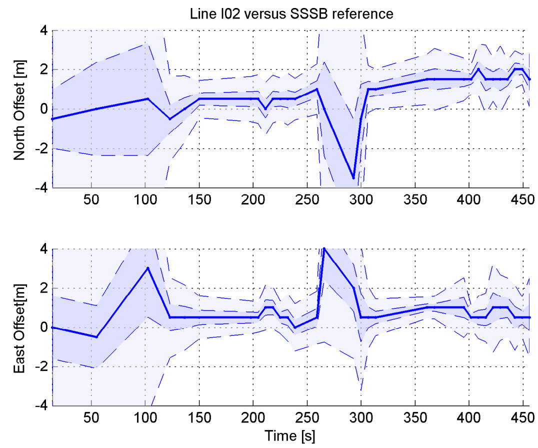

Fig. 10. Line l02: terrain navigation offset and confidence levels using PMF-nrm with SASB reference data from line l01.

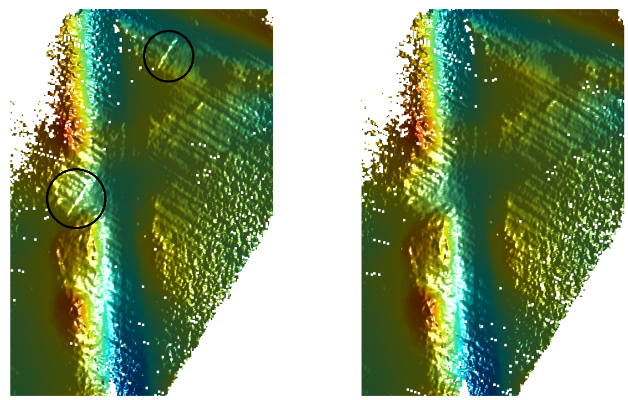

Fig. 11. SSSB bathy based on GPS-USBL aided INS in l03 (left) and terrain navigation aided INS in l03 (right).

normalization of the measurement likelihood function based on the number of measurements supported on the grid of the PMF, compared to a straightforward modification of the PMF. The accuracy obtained is probably sufficient for both large and small overlap lines, and the estimated accuracy seems to be conservative (a predicted side-effect to this particular modification of the PMF). We also found that the algorithm performance does not depend much on using a sidescan sonar bathymetry versus a synthetic aperture sonar bathymetry in the reference line. This means that it may suffice to use sidescan sonar bathymetry reference both in real-time (to ensure survey coverage and overlaps) and in post-processing of the AUV's navigation. The post-processed navigation can then be used to create a self-consistent high resolution bathymetric map using both interferometric SSS- and SAS-processing. This was demonstrated on the first lines in the survey where line-to-line terrain navigation was used to recreate the SSS bathymetry of the lines, removing inconsistencies in the overlaps that were present even in the GPS-USBL post-processed solution.

We will now focus our work on the integration of the relative position measurements from line-to-line terrain navigation with the INS, and the application of this in different survey patterns. Although the processing chain will be more complex, we will also consider estimating the position error by correlating SAS bathymetry between both lines. This may further increase the accuracy, as the measurements and the reference map will then have equal resolution.

Acknowledgment

The authors thank the crew onboard H.U. Sverdrup II and especially Ole Jacob Lorentzen at FFI for supervising the missions, and Einar Berglund at FFI for designing the patterns for these missions.

References

[1] B. Jalving, K. Gade, O. Hagen, and K. Vestgård, "A toolbox of aiding techniques for the HUGIN AUV integrated inertial navigation system," in *Proceedings of the IEEE OCEANS 2003*, San Diego, CA, USA, 2003.

[2] J. Carlstrøm, "Results from sea trials of the Swedish AUV62F's terrain navigation system," in *15th International International Symposium on Unmanned Untethered Submersible Technology (UUST'07)*, Durham, NH, USA, 2007.

[3] D. Meduna, S. Rock, and R. McEwen, "Closed-loop terrain relative navigation for auvs with non-inertial grade navigation sensors," in *2010 IEEE/OES Autonomous Underwater Vehicles (AUV)*, Monterey, CA , USA, 2010.

[4] G. Donovan, "Development and testing of a real-time terrain navigation method for auvs," in *OCEANS 2011*, 2011, pp. 1–9.

[5] O. K. Hagen, K. B. Ånonsen, and M. Mandt, "The HUGIN real-time terrain navigation system," in *Proceedings of the MTS/IEEE OCEANS 2010*, Seattle, WA, USA, 2010.

[6] S. Barkby, S. B. Williams, O. Pizarro, and M. V. Jakuba, "A featureless approach to efficient bathymetric slam using distributed particle mapping," *Journal of Field Robotics*, vol. 28, no. 1, pp. 19–39, 2011. [Online]. Available: http://dx.doi.org/10.1002/rob.20382

[7] C. Roman and H. Singh, "A self-consistent bathymetric mapping algorithm," *Journal of Field Robotics*, vol. 24, no. 1-2, pp. 23–50, 2007.

[8] K. Ånonsen and O. Hagen, "Recent developments in the hugin auv terrain navigation system," in *OCEANS 2011*. IEEE, 2011, pp. 1–7.

[9] D. K. Meduna, *Terrain relative navigation for sensor-limited systems with application to underwater vehicles*. Stanford University, 2011.

[10] P. E. Hagen, T. G. Fossum, and R. E. Hansen, "HISAS 1030: The Next Generation Mine Hunting Sonar for AUVs," in *UDT Pacific 2008 Conference Proceedings*, Sydney, Australia, November 2008.

[11] X. Lurton, *An Introduction to Underwater Acoustics: Principles and Applications*, 2nd ed. Chichester, UK: Springer Praxis Publishing, 2000.

[12] R. F. Hanssen, *Radar Interferometry: Data Interpretation and Error Analysis*. Dordrecht, The Netherlands: Kluwer Academic Publishers, 2001.

[13] T. O. Sæbø, R. E. Hansen, and A. Hanssen, "Relative height estimation by cross-correlating ground-range synthetic aperture sonar images," *IEEE J. Oceanic Eng.*, vol. 32, no. 4, pp. 971–982, October 2007.

[14] A. H. Quazi, "An overview on the time delay estimate in active and passive systems for target localization," *IEEE Trans. Acoust., Speech, Signal Processing*, vol. ASSP-29, no. 3, pp. 527–533, 1981.

[15] A. Bellettini and M. A. Pinto, "Theoretical accuracy of synthetic aperture sonar micronavigation using a displaced phase-center antenna," *IEEE J. Oceanic Eng.*, vol. 27, no. 4, pp. 780–789, 2002.

[16] T. O. Sæbø, S. A. V. Synnes, and R. E. Hansen, "Wideband Interferometry in Synthetic Aperture Sonar," *IEEE Trans. Geosci. Remote Sensing*, vol. 51, no. 8, pp. 4450–4459, August 2013.

[17] G. Franceschetti and R. Lanari, *Synthetic Aperture Radar Processing*. Boca Raton, FL, USA: CRC Press, 1999.

[18] P. Hagen, Ø. Hegrenæs, B. Jalving, Ø. Midtgaard, M. Wiig, and O. Hagen, *Underwater Vehicles*. Vienna, Austria: In-Tech Education and Publishing, 2009, ch. Making AUVs Truly Autonomous, pp. 129–152.

[19] K. B. Ånonsen, "Advances in terrain aided navigation for underwater vehicles," Ph.D. dissertation, Norwegian University of Science and Technology, 2010.

[20] R. Bucy, "Bayes theorem and digital realizations for non-linear filters," *The Journal of the Astronautical Sciences*, vol. XVII, no. 2, pp. 80–94, Sep.-Oct. 1969.

[21] S. Dektor and S. Rock, "Improving robustness of terrain-relative navigation for auvs in regions with flat terrain," in *Autonomous Underwater Vehicles (AUV), 2012 IEEE/OES*. IEEE, 2012, pp. 1–7.

[22] ——, "Robust adaptive terrain-relative navigation," in *Oceans-St. John's, 2014*. IEEE, 2014, pp. 1–10.

[23] K. Gade, "NavLab, a generic simulation and post-processing tool for navigation," *European Journal of Navigation*, vol. 2, no. 4, pp. 51–59, November 2004.

[24] O. K. Hagen, K. B. Ånonsen, and T. O. Sæbø, "Low altitude AUV terrain navigation using an interferometric sidescan sonar," in *Proceedings of the MTS/IEEE OCEANS 2011*, Kona,HI,USA, 2011.